

See discussions, stats, and author profiles for this publication at: <https://www.researchgate.net/publication/43532310>

Compressive Stress Effect on the Radial Elastic Modulus of Oxidized Si Nanowires

ARTICLE *in* NANO LETTERS · JUNE 2010

Impact Factor: 13.59 · DOI: 10.1021/nl100062n · Source: PubMed

CITATIONS

23

READS

27

4 AUTHORS, INCLUDING:



[Sergiy Krylyuk](#)

National Institute of Standards and Techn...

63 PUBLICATIONS 497 CITATIONS

SEE PROFILE



[Albert Davydov](#)

National Institute of Standards and Techn...

146 PUBLICATIONS 1,994 CITATIONS

SEE PROFILE

Compressive Stress Effect on the Radial Elastic Modulus of Oxidized Si Nanowires

G. Stan,^{*,†} S. Krylyuk,^{§,†} A. V. Davydov,[§] and R. F. Cook[†]

[†]Ceramics Division and [§]Metallurgy Division, National Institute of Standards and Technology, Gaithersburg, Maryland 20899

ABSTRACT Detailed understanding and optimal control of the properties of Si nanowires are essential steps in developing Si nanoscale circuitry. In this work, we have investigated mechanical properties of as-grown and oxidized Si nanowires as a function of their diameter. From contact-resonance atomic force microscopy measurements, the effect of the compressive stress at the Si–SiO₂ interface was revealed in the diameter dependence of the elastic modulus of Si nanowires oxidized at 900 and 1000 °C. A modified core–shell model that includes the interface stress developed during oxidation captures the diameter dependence observed in the measured elastic moduli of these oxidized Si nanowires. The values of strain and stress as well as the width of the stressed transition region at the Si–SiO₂ interface agree with those reported in simulations and experiments.

KEYWORDS Nanowires, nanoscale elastic modulus, interface stress, contact resonance atomic force microscopy

The synthesis and processing of materials into nanostructures open avenues to further advance and diversify current electronic, optoelectronic, and sensor applications.¹ Among these systems, Si nanowires (NWs) are distinctly remarkable as they bring the previous decades' knowledge of silicon technology into nanoscale applications. Fabricated by both bottom-up^{2,3} and top-down,⁴ as well as selective bridging⁵ methods, Si NWs have been shown to possess exceptional electrical,^{6,7} optical,^{8,9} mechanical,^{10,11} piezoelectric,¹² and thermoelectric properties^{13,14} as required for building blocks in future nanodevice integration.

The relevance of Si nanoscale mechanical properties has been recognized not only in devices with direct mechanical functionality^{10,12} but also in current and future high-speed Si-based electronics (e.g., epitaxial Si–Ge layers,¹⁵ oxidized Si NWs¹⁶) through the strain-controlled mobility of carriers. In high-density planar structures, however, simple scaling dictates that strain modification of electron mobility will cease to be effective as dimensions shrink.¹⁵ An alternative to such structures is offered by nonplanar nanostructures with built-in stress, such as Ge nanostressors on silicon-on-insulator substrates¹⁷ or oxidized Si NWs.^{16,18} From this perspective, the characterization and understanding of the mechanical properties of nonplanar Si–SiO₂ interfaces are of significant utility in the development of Si nanostructures for Si-based integrated circuits.^{18,19}

To address mechanical property measurements at the nanoscale, various concepts and techniques have been developed in the past few years: electromechanical resonance,²⁰ tensile tests,²¹ three-point bending tests,²² nanoin-

dentation,²³ and contact-resonance atomic force microscopy,²⁴ for example. Among these techniques, contact-resonance atomic force microscopy (CR-AFM)^{25,26} distinguishes itself through a simple and versatile experimental setup (substrate-supported specimens as for AFM measurements), accurate, precise, and nondestructive elastic modulus measurements in the range of gigapascals to hundreds of gigapascals,^{27,28} and direct property–topography correlation.²⁹ In this work, as-grown Si NWs (with negligible oxide shell) and Si NWs oxidized at different temperatures (with oxide shells in the range 10–30 nm thick) and of various diameters were measured by CR-AFM to determine their radial elastic moduli. With precise knowledge of the Si core and SiO₂ shell dimensions, the observed size dependence of the measured elastic modulus is resolved by considering the stress contribution to the elastic modulus of the oxidized Si NWs.

The elastic moduli of the investigated NWs supported on a Si substrate were determined by load-dependent CR-AFM.²⁷ Once a NW was localized on the substrate, measurements were performed along a direction perpendicular to the length of the NW (refer to Figure 1 for the measurement configuration). Along this path (dotted line in Figure 1), the measurements were performed from point to point by starting away from the NW, passing over the NW, and ending on the other side of the NW. This new proposed measurement procedure provides a few advantages. First, by starting and ending on the substrate, the contact geometry preservation is verified during measurements and the baseline for measurement calibration assured. Second, the radial elastic modulus is probed at various locations across the NW. Third, the load-dependent CR-AFM measurements allow the use of smaller applied loads than in single-load CR-AFM; also the result of such measurements is a more precise average value of the elastic modulus.²⁷

* To whom correspondence should be addressed, gheorghe.stan@nist.gov.

[†] On leave from Institute of Semiconductor Physics, National Academy of Sciences of Ukraine, Kiev, Ukraine.

Received for review: 01/8/2010

Published on Web: 04/30/2010



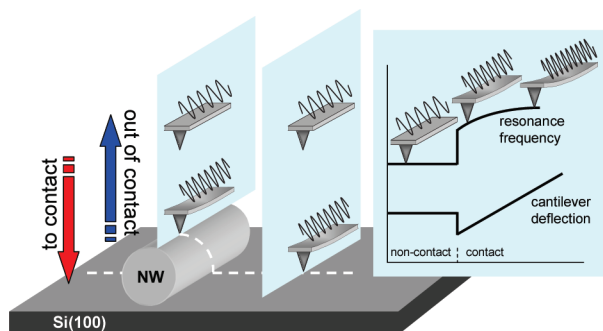


FIGURE 1. Load-dependent CR-AFM measurements were performed along a direction perpendicular to an investigated NW. At points along this path (dotted trace), on the substrate as well as over the NW, the resonance frequency and deflection of the cantilever were both recorded as the probe was gradually brought in and out of contact with the sample tested. The resonance frequency changes as a function of material probed (substrate or NW), contact geometry, and applied force.

Three different sets of NWs were used in this study: (1) as-grown Si NWs; (2) Si NWs oxidized at 900 °C for 5 min; and (3) Si NWs oxidized at 1000 °C for 5 min. Initially, all the Si NWs were synthesized by a Au-catalytic vapor–liquid–solid technique on Si(111) substrates at 500 °C in a mixture of SiH₄, N₂, and H₂ gases. From electron diffraction in transmission electron microscopy (TEM) and electron backscatter diffraction, the NWs were found to be single crystal with their axis along the Si $\langle 112 \rangle$ direction. Subsequently, some of the NWs were oxidized at different temperatures through a rapid thermal oxidation and turned into coaxial Si core–SiO₂ shell structures. The structure and morphology of oxidized Si NWs from the same batches as those used here were investigated in detail in ref 30 by TEM. From TEM images of individual NWs, the thicknesses of the Si core and SiO₂ shell were measured. In Figure 2, these results³⁰ are summarized for Si NWs oxidized at 900 °C for 5 min and Si NWs oxidized at 1000 °C for 5 min. For both types of NWs, the oxide thickness versus NW radius exhibits a linear dependence but with a different slope. The best-fit linear dependencies in Figure 2 lead to simple forms for the ratio, $\beta = r_{\text{core}}/R_{\text{NW}}$, of the NW core radius, r_{core} , to the total NW radius, R_{NW} : $\beta = 0.81 - 6.1/R_{\text{NW}}$ (nm) and $0.87 - 25.5/R_{\text{NW}}$ (nm) for $R_{\text{NW}} > 15$ nm and $R_{\text{NW}} > 30$ nm, for the NWs oxidized at 900 and 1000 °C, respectively. These core–shell geometry ratios will be used later in analysis of the NW modulus. For CR-AFM measurements, the NWs were released from their growth substrate by ultrasonic agitation in isopropyl alcohol and the NW solution formed was then dispersed on Si(100) substrates and dried.

The additional instrumentation (LabVIEW, National Instruments, Austin, TX)³¹ required for CR-AFM measurements was attached to a commercial AFM (MultiMode V, Veeco Instruments, Santa Barbara, CA)³¹ as described elsewhere.^{24,27} The AFM probes (PPP-SEIH, NanoSensors, Neuchatel, Switzerland)³¹ used were single-crystal Si cantilevers with integrated tips; the cantilever spring constant, 8

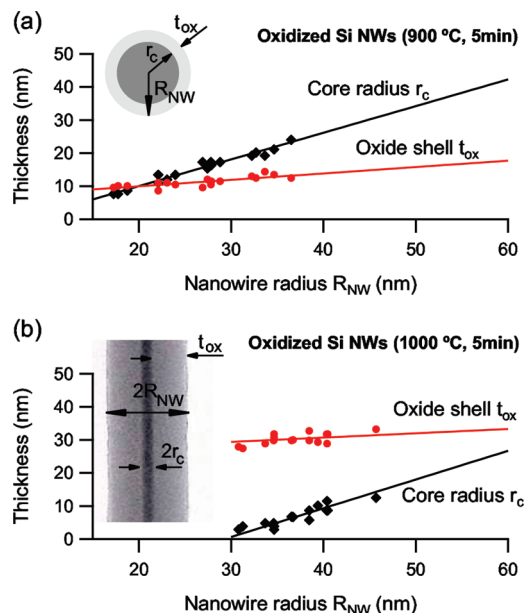


FIGURE 2. The NW radius dependencies of the Si core and SiO₂ shell thickness for (a) Si NWs oxidized at 900 °C for 5 min and (b) Si NWs oxidized at 1000 °C for 5 min. The insets are (a) a top view diagram of the NW core–shell structure and (b) a transmission electron microscope image of an oxidized Si NW (1000 °C, 5 min) with radius 36.5 nm.

$\text{N m}^{-1} < k_c < 12 \text{ N m}^{-1}$, was determined for each probe by the thermal method procedure provided with the AFM software. In each set of measurements, the tip radius was determined by deconvoluting the tip effect to the AFM topographic profile over the NWs measured. Values in the range of 15–30 nm were found for different tips used. A 20% uncertainty in the tip radius was included in the calculations involving this parameter. During approach and retract probe displacement ramps, the applied load was adjusted through the AFM force-displacement routine, with the maximum applied load controlled by the AFM trigger set point.

The quantity provided by CR-AFM measurements for elastic modulus calculation is the normal tip–sample contact stiffness.^{25,26} This normal contact stiffness (hereafter referred to as contact stiffness) is defined by the z derivative of the contact force acting normally on the plane of contact, where the z direction is normal to the contact plane. To measure the contact stiffness, at each location, the deflection and resonance frequency of the cantilever were recorded as a function of the AFM “ z -piezo” displacement while the tip is brought in and out of contact.²⁷ Prior to CR-AFM measurements on a selected NW, the NW and its surrounding area were mapped by low-speed force-displacement measurements. In Figure 3 are shown such data collected around a Si NW oxidized at 900 °C for 5 min, about 50 nm in diameter. From force-displacement measurements performed at a frequency of 1 Hz, strip maps of force-displacement slope (Figure 3a) and adhesive force (Figure 3b) were constructed around the investigated NW. In both maps the

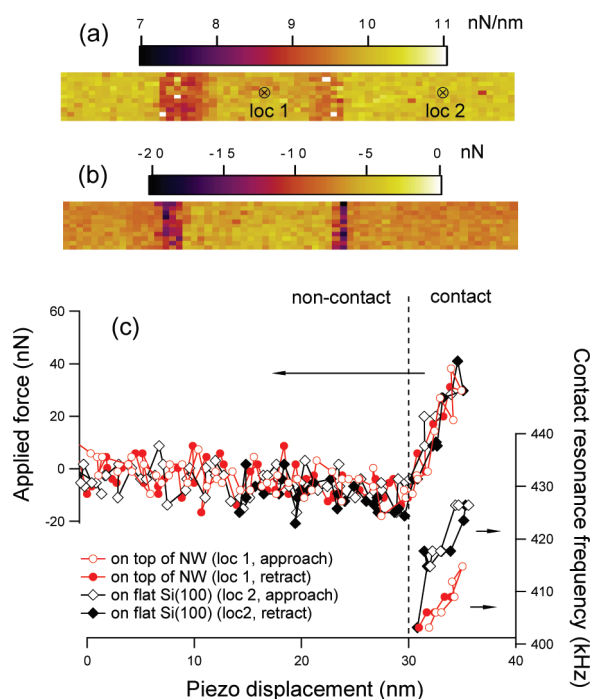


FIGURE 3. 250 nm × 50 nm strip maps of (a) the slope of the cantilever deflection versus piezo displacement and (b) pull-off force acquired at 1 Hz frequency on and around a 50 nm diameter oxidized Si NW (900 °C, 5 min). (c) At the locations marked in (a), the cantilever deflection and resonance frequency were recorded as the AFM tip was brought in and out of contact. In the noncontact region, the free-air resonance frequency of the cantilever was 106.3 kHz, outside of the frequency sweep range (300–500 kHz) used here.

NW edges are clearly localized by the large perturbations that occurred in the cantilever response as a result of unstable contact geometry at these positions; these locations will be excluded from our subsequent analysis. As can be seen in Figure 3a, no strong contrast was observed between substrate and NW, which means that, for the materials probed here, the force-displacement slope is not sensitive enough to be used for contact stiffness calculation. A small contrast of about 1 nN was observed in the adhesive force map from substrate (6.8 ± 1.0 nN) to NW (5.5 ± 0.9 nN). However, as can be seen in Figure 3c, the force-displacement responses acquired in CR-AFM show no difference in the pull-off force most likely due to the adhesive force alteration caused by the high-speed small-amplitude dithering of the cantilever.²⁷ The main benefit provided by CR-AFM measurements comes from the contrast in the contact resonance frequency. This can be seen in Figure 3c in which are shown both the deflection and resonance frequency of the cantilever from two tip excursions: one on top of the NW and one on the substrate. At each indentation depth, the contact resonance frequency was determined by sweeping the cantilever's driving frequency in the 300–500 kHz range. Unlike deflection versus displacement curves, a clear contrast is observed in the contact region for the resonance versus displacement responses on the NW and Si substrate.

As the piezo-displacement is uniquely converted into the applied force within the contact region, the two data sets can be combined into a contact resonance frequency versus applied force response. With a known elastic modulus for the substrate, the distinct contrast between the two contact resonance frequency versus applied force curves, on the NW and substrate, can then be converted into the elastic modulus of the NW.

To convert the measurements into radial elastic modulus, cantilever dynamics and contact mechanics models describing the system are used. At every location, the cantilever dynamics changes as the tip is brought in and out of contact and its resonance frequency shifts up or down as the applied force increases or decreases. By modeling the cantilever as a clamped-spring coupled beam,²⁵ this frequency shift is converted into contact stiffness, so contact stiffness versus applied force curves are generated at each location. Besides the applied force, two other contributions modify the contact stiffness: (i) the contact geometry, which is spherical apex-on-flat over the Si substrate and spherical apex-on-cylinder over the NW, and (ii) the elastic properties of the materials probed. In the framework of Hertzian contact mechanics,³² the contact stiffness between the spherical tip of radius R_T and a cylindrical NW of radius R_{NW} reduces to

$$k_{\text{tip-NW}}^* = (6R_T E_T^* \sqrt{1 - (x/R_{NW})^2} / \gamma)^{1/3} \quad (1)$$

with the geometrical factor $\gamma = 2(1 - e^2)K^3(e)(2R_{NW} + R_T) / \pi^2 E(e) R_{NW}$ depending on the tip and NW radii, the complete elliptic integrals $K(e)$ and $E(e)$ of first and second kind, and the eccentricity e of the ellipse of contact.²⁴ As the tip moves over the cylindrical nanowire, the normal contact force F_n deviates from the magnitude and direction of the applied force F . This change is considered in eq 1 through the cosine of the angle formed by F and F_n , $(1 - (x/R_{NW})^2)^{1/2}$, with x being the horizontal distance between the tip and the NW center. On the substrate, eq 1 reduces to the tip-on-flat contact stiffness formula

$$k_{\text{tip-substrate}}^* = (6R_T E_T^*)^{1/3} \quad (2)$$

In both eqs 1 and 2, the effective elastic modulus E^* is a combination of the indentation moduli of the tip, M_T , and the nanowire or substrate, M_{NW} or M_S , respectively

$$\frac{1}{E_{T-NW,S}^*} = \frac{1}{M_T} + \frac{1}{M_{NW,S}} = \frac{1 - \nu_T^2}{E_T} + \frac{1 - \nu_{NW,S}^2}{E_{NW,S}} \quad (3)$$

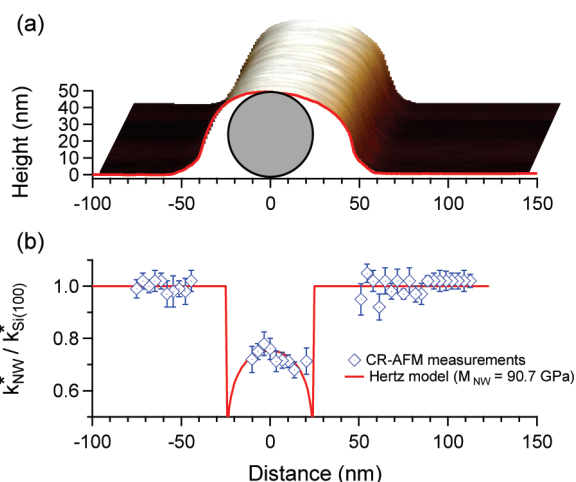


FIGURE 4. (a) The three-dimensional profile of an oxidized Si NW (900 °C, 5 min) on a Si(100) substrate. (b) The CR-AFM measurements are shown here in the form of contact stiffness ratio, $k_{\text{tip-NW}}^*/k_{\text{tip-substrate}}^*$. A set of such contact stiffness ratios was calculated for a few applied forces during approaching and retracting. The error bars are 1 standard deviation of the load-dependent measurements performed at each location. The elastic modulus of the NW was adjusted in the Hertz model calculation for the best fit of the measurements over the NW, e.g., 90.7 ± 5.2 GPa in this case.

E and ν are Young's modulus and Poisson's ratio of the materials indicated by their subscript indices: T for the tip, NW for the nanowire, and S for the substrate.

The ratio of the contact stiffnesses on the nanowire and substrate is readily obtained from eqs 1 and 2

$$\frac{k_{\text{tip-NW}}^*}{k_{\text{tip-substrate}}^*} = \left(\frac{\sqrt{1 - (x/R_{\text{NW}})^2}}{\gamma} \right)^{1/3} \left(\frac{E_{\text{T-NW}}^*}{E_{\text{T-S}}^*} \right)^{2/3} \quad (4)$$

As can be seen from eq 4, the ratio $k_{\text{tip-NW}}^*/k_{\text{tip-substrate}}^*$ does not depend on the applied force but only on the contact geometry (first parentheses) and elastic properties of the materials (second parentheses). Indeed, at each location, no significant variations were observed in the contact stiffness ratio calculated from measurements made at different applied forces and an average value of this ratio was considered. This approach is valid as long as the adhesive forces on the NW and substrate are negligible or comparable (as observed in Figure 3b); if significant, the contribution of the adhesive forces can also be included.²⁷

In Figure 4 there are shown the topography (Figure 4a) and contact stiffness measurements (Figure 4b) performed across an investigated NW. At each location, an average contact stiffness was determined from measurements made when the applied force was ramped in the range from the maximum applied force to the maximum less approximately 50 nN. As shown in Figure 4b, these average contact stiffnesses were then normalized to the average contact stiffness determined on the flat Si(100). Good correlation

was observed between the topography and contact stiffness profile as the tip was moved across the NW. Within the frequency sweep range (300–500 kHz), no CR-AFM response was detected at the NW edges where the mechanics of the probe–cantilever system was strongly perturbed. The lack of a well-established contact geometry at these edge locations was also confirmed by the large amplitude perturbations observed in the lateral deflection of the cantilever. As such, only a partial curvature dependence was recovered for the contact stiffness over the NW. By using eqs 3 and 4 with M_{NW} as the fit parameter, the theoretical profile for the contact stiffness ratio over the NW was adjusted to fit the experimental points. In these calculations, the indentation modulus of the reference Si(100) has been considered to be 164.8 GPa, calculated as in ref.³³ For homogeneous NWs, as-grown and fully oxidized Si NWs, the radial indentation modulus M_{NW} (or conversely the Young's modulus E_{NW}) is the final quantity determined from such CR-AFM measurements.

In the case of oxidized Si NWs, individual contributions of the Si core and oxidized SiO₂ shell to the elastic modulus of the NW can be further separated through a simple core–shell model.²⁴ In addition to these core and shell contributions, we also have to consider the contribution from the narrow, high-density interface transformation region,^{34–36} in which the oxidation takes place and in which a difference in the mechanical properties is expected due to the large compressive stress developed during oxidation. The origin of the stress developed at the Si–SiO₂ interface during oxidation resides in the difference between the volumes of consumed Si and newly formed SiO₂; the ratio of these volumes being approximately equal to 20/45, the ratio of the atomic volume of Si and the molecular volume of SiO₂. As the oxide is progressively formed at the Si–SiO₂ interface, it is pushed outward and a radial compressive stress is developed at the interface and decays toward the free surface of the oxide.³⁸ In planar structures, this stress extends biaxially in the oxidation plane and bends the interface.³⁷ The effect is even more pronounced at curved Si–SiO₂ interfaces leading to retarded and self-limited oxidation in structures of large curvatures such as silicon NWs of small radius. The large compressive stress developed during the nonplanar two-dimensional deformation of the formed oxide hinders the oxide growth mostly through a severe suppression of oxygen diffusion.³⁶ It has been shown that this compressive stress is released through SiO₂ viscous flow if the oxidation takes place at temperatures higher than about 960 °C (the viscous flow point of SiO₂).³⁷ The presence of residual stress in oxidized Si NWs has been probed experimentally by observing the shift of the optical phonon peak in Raman spectra of oxidized Si NWs before and after removing the oxide shell.^{16,18,39}

The large strain and associated large compressive stress accumulated during oxidation lead to an interface rim (annular tube) between the oxidized SiO₂ NW shell and unoxidized Si NW core with elastic properties that differ

from both the core and shell, and which affect the overall NW modulus. An estimation of the thickness, δ_{rim} , of this narrow region around the interface can be obtained by solving the Lamé's strain potential in a core-shell cylindrical structure (see for example ref 40). The free expansion implied by the consideration of the atomic and molecular volumes on oxidation is constrained by the requirement of strain compatibility at the interface. As a consequence, the core and shell exhibit radial displacements on oxidation, with a decrease in the outer radius of the core and an increase in the inner radius of the shell from the unconstrained values. The sum of these displacements provides an estimate of the rim thickness

$$\frac{\delta_{\text{rim}}}{r_{\text{core}}} = \left[\frac{1 - \nu_{\text{core}}}{E_{\text{core}}} + \left(\frac{R_{\text{NW}}^2 + r_{\text{core}}^2}{R_{\text{NW}}^2 - r_{\text{core}}^2} + \nu_{\text{shell}} \right) \frac{1}{E_{\text{shell}}} \right] \sigma_i \quad (5)$$

with σ_i the stress at the Si-SiO₂ interface. The elastic modulus of the rim is calculated from the stress/strain ratio at the interface:

$$E_{\text{rim}} = (1 - \nu_{\text{rim}}) r_{\text{core}} \sigma_i / \delta_{\text{rim}} \quad (6)$$

where $\varepsilon_i = \delta_{\text{rim}}/r_{\text{core}}$ is the characteristic radial strain associated with the formation of the rim at the core boundary. With the additional contribution of the rim to the simple core-shell model,²⁴ the resulting elastic modulus of the NW is obtained by considering the cylindrical contributions of the core, rim, and shell

$$\left(\frac{1 - \nu}{E} \right)_{\text{NW}} R_{\text{NW}} = \left(\frac{1 - \nu}{E} \right)_{\text{core}} r_{\text{core}} + \left(\frac{1 - \nu}{E} \right)_{\text{rim}} \delta_{\text{rim}} + \left(\frac{1 - \nu}{E} \right)_{\text{shell}} t_{\text{ox}} \quad (7)$$

with t_{ox} the thickness of the oxide shell and $r_{\text{core}} = R_{\text{NW}} - t_{\text{ox}} - \delta_{\text{rim}} \approx R_{\text{NW}} - t_{\text{ox}}$. Equations 5 to 7 may be combined along with the definition of β to give

$$\left(\frac{1 - \nu}{E} \right)_{\text{NW}} = \beta \left(\frac{1 - \nu}{E} \right)_{\text{core}} + (1 - \beta) \left(\frac{1 - \nu}{E} \right)_{\text{shell}} + \beta \left[\left(\frac{1 - \nu}{E} \right)_{\text{core}} + \left(\frac{1 + \beta^2}{1 - \beta^2} + \nu_{\text{shell}} \right) \frac{1}{E_{\text{shell}}} \right] \sigma_i \quad (8)$$

which provides a prediction of the NW modulus as a function of the NW geometry, the core and shell elastic properties, and the stress at the core-shell interface in the rim. The assumption made in generating this prediction is that the

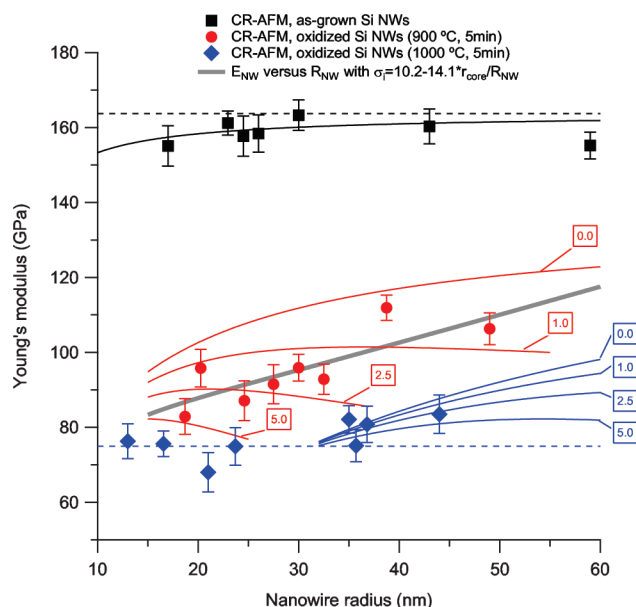


FIGURE 5. The Young's modulus of as-grown and oxidized Si NWs of various radii. The values determined for the Young's modulus of as-grown Si NWs and fully oxidized Si NWs scatter around the bulk values of the elastic modulus of these materials, 164 GPa for Si(112) and 75 GPa for SiO₂ (dotted lines). The simple core-shell model (no interface stress) suggests a slight radius dependence for the elastic modulus of as-grown Si NWs (black curve). In the case of oxidized Si NWs, the Young's modulus vs NW radius dependence is explained by considering the contribution from the Si-SiO₂ interface compressive stress; the red and blue continuous curves are calculated based on eq 8 for the Si NWs oxidized at 900 and 1000 °C, respectively. The numbers tagged to each curve show the interface compressive stress σ_i for which the curves were calculated. The thick gray curve was obtained when σ_i was considered to be radius dependent (see text for details).

NW is in mechanical equilibrium at all stages of oxidation, i.e., that oxygen diffusion is slow relative to strain and stress adjustment in the NW. This modified core-shell model is used in the following to interpret the radial dependence of the elastic modulus of partially oxidized Si NWs.

The above measurement procedure and data analysis were followed on NWs of different radii from each set of oxidation conditions. As can be seen in Figure 5, the determined elastic moduli separate into distinct bands for each set. For the as-grown Si NWs the measured values approach the average bulk value of the elastic modulus in the (112) plane, 163.7 GPa; the average Poisson's ratio in the (112) plane of the Si is 0.239 (see ref 41 for calculation). The uncertainties of the calculated elastic modulus values in Figure 5 originated from the uncertainties associated with the fit calculation of the contact stiffness dependence over each NW probed (example shown in Figure 4). A slight reduction is observed at small radii, which can be fitted by considering the contribution of a thin 0.5 nm oxide surface layer to the elastic modulus of NWs (eq 7 without rim contribution). However, this may not be the most accurate estimation of the oxide thickness on the as-grown Si NWs because such a native oxide layer was also present on the Si(100) substrate and much of its contribution would

have canceled out through the measurement calibration. The radial elastic modulus of Si NWs as determined here from CR-AFM measurements compares well with that found from tensile tests performed on individual Si NWs, of comparable diameters.⁴²

For Si NWs oxidized at 1000 °C for 5 min, the determined Young's modulus (calculated from measurements by means of eqs 1–4) was around 75 GPa for NWs with radius less than 30 nm (refer to Figure 5). According to the shell and core radius dependencies shown in Figure 2b, the Si NWs oxidized at 1000 °C for 5 min are completely oxidized when their radius is less than 30 nm. Consequently the value of 75 GPa has been considered as the Young's modulus of the NW SiO₂ shells; the Poisson's ratio of SiO₂ was taken to be 0.178. The Young's modulus determined here for SiO₂ NWs is in the reported range of the elastic modulus of amorphous SiO₂ NWs, 76.6 ± 7.2 GPa, as measured by three-point bending tests.⁴⁵ A slight increase in the elastic modulus is observed for these NWs when their radius was larger than 30 nm, in this case a core contribution to the elastic modulus being expected. However, the measurement uncertainty prevents an assessment of any interface Si–SiO₂ stress influence on the elastic modulus of these NWs, the simple core–shell model (without rim contribution) also providing a good description. Also, it is possible that, due to viscoelastic flow,^{18,38} the oxide shell could have been entirely relaxed at this oxidation temperature.

Completely different behavior was observed for the Young's modulus of the Si NWs oxidized at 900 °C for 5 min. The Young's modulus of these NWs varied from 80 to 110 GPa as their radius ranged from 15 to 50 nm. These values are greater than those for the SiO₂ Young's modulus and less than those predicted by the simple core–shell model. The theoretical curves start to fit the measurements when a compressive stress effect is considered at the Si–SiO₂ interface through eq 8. As the NW radius increased, the oxide shell became thicker (Figure 2a), which implies that the interface stress should decrease as the curvature decreased and a less deformed oxide was accommodated.^{38,44} Indeed, this behavior can be identified here in the radial dependence of the elastic modulus of Si NWs oxidized at 900 °C for 5 min. As shown in Figure 5, interface stresses around 2.5 GPa predict a Young's modulus around 90 GPa for those NWs of radius between 15 and 30 nm. For radii larger than 30 nm, the elastic modulus increases in magnitude and the interface stress diminishes significantly, the theoretical curves fitting the measurements for stresses between 0 and 1 GPa. This radius dependence of the interface stress can be empirically considered for the elastic moduli calculated by eq 8. Thus, from data shown in Table 1, the interface stress of Si NWs oxidized at 900 °C for 5 min decreases with the increase of β ratio as $\sigma_i = 10.2 - 14.1\beta$, for NWs with radius in the 20–50 nm range. On considering this radius dependence of the interface stress in the expression for the elastic modulus, a more precise data trend is conveyed for

TABLE 1. The Young's Modulus As Determined from CR-AFM Measurements for a Few Si NWs Oxidized at 900 °C for 5 min^a

R_{NW} (nm)	β ($r_{\text{core}}/R_{\text{NW}}$)	E_{NW} (GPa)	ϵ_i (%)	σ_i (GPa)	δ_{rim} (nm)
18.7	0.48	82.9	12.8	4.5	1.1
20.3	0.50	95.8	3.8	1.3	0.4
24.6	0.56	87.1	9.7	3.0	1.3
27.5	0.58	91.5	7.5	2.2	1.2
30.0	0.60	95.9	5.5	1.6	1.0
32.5	0.62	92.9	6.8	1.9	1.4
38.9	0.65	111.9	1.1	0.3	0.3
49.0	0.68	106.3	2.0	0.7	1.0

^a The compressive strain and stress and thickness of the transition region in the vicinity of the Si–SiO₂ interface were estimated based on a modified core–shell model (see eq 8).

the measured elastic modulus of Si NWs oxidized at 900 °C for 5 min (solid thick gray curve in Figure 5). An average Poisson's ratio $\nu_{\text{NW}} = 0.2$ was assumed in calculating E_{NW} from eq 8.

The Si–SiO₂ interface compressive stress and strain deduced here (refer to Table 1) from elastic modulus measurements are of the same order of magnitude as those found in simulations that model the expansion of the SiO₂ around thermally oxidized Si nanostructures. Either in two-dimensional continuum approximation simulations⁴⁵ that specifically account for the transition region where Si is converted in SiO₂ or three-dimensional molecular dynamics simulations,⁴⁶ regions of large strain (1 % to 2 %) and stress (1 to 6 GPa) were calculated in the vicinity of the Si–SiO₂ interface of oxidized Si NWs. It is also worth mentioning that, from eq 5, the transition region within which the stress progressively accumulated during oxidation was found to extend over nanometer distance from the Si–SiO₂ interface (see the last column in Table 1). Similarly, in simulations,^{46,47} the large compressive stress near the Si–SiO₂ interface has been shown to be within a transition region of 1–2 nm. Experimentally, the existence of a high-density layer of thickness up to 1.5 nm at the Si–SiO₂ interface was probed by high-accuracy X-ray reflectivity measurements.^{34,35}

This study illustrates the principle of using mechanical property measurements, in this case of the NW indentation modulus, to infer a nanoscale structural attribute, in this case the nature of the oxidation transformation zone within the NW. Other studies based on the same principle include those in which measurement of the development of thin film stresses was used to infer the nature of nanoscale defect structures in vapor-deposited thin films.^{48,49} In the latter case, the desorption of H from silicon oxide, nitride, or oxynitride films⁴⁸ or the exsolution of Ar from aluminum oxide films,⁴⁹ imposed a negative dilatation in the film that was constrained by an underlying substrate leading to a tensile reaction stress in the film. In the case here, absorption of O into the Si NWs imposed a positive dilatation in a transformation rim that was constrained by adjacent core and shell leading to a compressive reaction stress in the NW. In both cases, thermochemical instability of the system leads to nanoscale strains and thus a coupling to mechanical

responses and properties, although the approach to full thermodynamic equilibrium for the two cases differs: In the thin-film case, diffusion is rapid and hence the time rates of change of mechanical properties are controlled by H desorption or Ar exsolution reaction kinetics.^{48,49} In the NW case, the oxidation reaction is rapid and hence the time rate of change of the mechanical properties is controlled by the kinetics of diffusion, which may in turn be influenced by the state of mechanical stress.³⁸

In conclusion, CR-AFM measurements were performed on as-grown and oxidized Si NWs and the radial elastic modulus determined as a function of NW radius. Radius-independent values were observed for the elastic modulus of as-grown and fully oxidized Si NWs. For these NWs, the elastic moduli determined from CR-AFM measurements are in the same range as those found in tensile tests on single-crystal Si NWs⁴² and three-point bending tests on amorphous SiO₂ NWs,⁴³ respectively. In the case of partially oxidized Si NWs, the radius dependence of the elastic modulus was explained through a modified core-shell model that includes the contribution from the mechanically modified Si-SiO₂ interface. The Si-SiO₂ interface strain and stress, inferred here from the elastic response of Si NWs oxidized at 900 °C, are of the same order of magnitude as those reported in simulations^{45,46} and Raman spectra measurements.^{16,18,39} The great advantage of the present investigation is it provides local stress evaluation on nanoscale locations accessed by AFM. In much the same way, the applicability of CR-AFM can be extended for probing stressed interface regions in other nanoscale heterostructures.

Acknowledgment. The authors thank Dr. Igor Levin from the National Institute of Standards and Technology for providing TEM characterization of the Si NWs.

REFERENCES AND NOTES

- (1) Lieber, C. M.; Wang, Z. L. *MRS Bull.* **2007**, *32*, 99.
- (2) Morales, A. M.; Lieber, C. M. *Science* **1998**, *279*, 208.
- (3) Fuhrmann, B.; Leipner, H. S.; Höche, H.-R.; Schubert, L.; Werner, P.; Gösele, U. *Nano Lett.* **2005**, *5*, 2524.
- (4) Stern, E.; Klemic, J. F.; Routenberg, D. A.; Wyrembak, P. N.; Turner-Evans, D. B.; Hamilton, A. D.; LaVan, D. A.; Fahmy, T. M.; Reed, M. A. *Nature* **2007**, *445*, 519.
- (5) He, R. R.; Gao, D.; Fan, R.; Hochbaum, A. I.; Carraro, C.; Maboudian, R.; Yang, P. D. *Adv. Mater.* **2005**, *17*, 2098.
- (6) Cui, Y.; Duan, X.; Hu, J.; Lieber, C. M. *J. Phys. Chem. B* **2000**, *104*, 5213.
- (7) Duan, X.; Niu, C.; Sahi, V.; Chen, J.; Wallace Parce, J.; Empedocles, S.; Goldman, J. L. *Nature* **2003**, *425*, 274.
- (8) Huang, Y.; Duan, X.; Lieber, C. M. *Small* **2005**, *1*, 142.
- (9) Tian, B.; Zheng, X.; Kempa, T. J.; Fang, Y.; Yu, N.; Yu, G.; Huang, J.; Lieber, C. M. *Nature* **2007**, *449*, 885.
- (10) Feng, X. L.; He, R.; Yang, P.; Roukes, M. L. *Nano Lett.* **2007**, *7*, 1955.
- (11) Han, X.; Zheng, K.; Zhang, Y.; Zhang, X.; Zhang, Z.; Wang, Z. L. *Adv. Mater.* **2007**, *19*, 2112.
- (12) He, R. R.; Yang, P. D. *Nat. Nanotechnol.* **2006**, *1*, 42.
- (13) Hochbaum, A. I.; Chen, R.; Delgado, R. D.; Liang, W.; Garnett, E. C.; Najarian, M.; Majumdar, A.; Yang, P. *Nature* **2008**, *451*, 163.
- (14) Boukai, A. I.; Bunimovich, Y.; Tahir-Kheli, J.; Yu, J.-K.; Goddard, W. A., III; Heath, J. R. *Nature* **2008**, *451*, 168.
- (15) Chidambaram, P. R.; Bowen, C.; Chakravarthi, S.; Machala, C.; Wise, R. *IEEE Trans. Electron Devices* **2006**, *53*, 944.
- (16) Seike, A.; Tange, T.; Sano, I.; Sugiura, Y.; Kosemura, D.; Ogura, A.; Ohdomari, I. *Appl. Phys. Lett.* **2007**, *91*, No. 062108.
- (17) Liu, F.; Huang, M.; Rugheimer, P. P.; Savage, D. E.; Lagally, M. G. *Phys. Rev. Lett.* **2002**, *89*, 136101.
- (18) Najmzadeh, M.; Bouvet, D.; Dobrosz, P.; Olsen, S.; Ionescu, A. M. *Microelectron. Eng.* **2009**, *86*, 1961.
- (19) Dong, Y.; Yu, G.; McAlpine, M. C.; Lu, W.; Lieber, C. M. *Nano Lett.* **2008**, *8*, 386.
- (20) Poncharal, P.; Wang, Z. L.; Ugarte, D.; de Heer, W. A. *Science* **1999**, *283*, 1513.
- (21) Yu, M. F.; Lourie, O.; Dyer, M. J.; Moloni, K.; Kelly, T. F.; Ruoff, R. S. *Science* **2000**, *287*, 637.
- (22) Salvétat, J. P.; Kulik, A. J.; Bonard, J. M.; Briggs, G. A. D.; Stöckli, T.; Métrier, K.; Bonnamy, S.; Béguin, F.; Burnham, N. A.; Forro, L. *Adv. Mater.* **1999**, *11*, 161.
- (23) Li, X.; Gao, H.; Murphy, C. J.; Caswell, K. K. *Nano Lett.* **2003**, *3*, 1495.
- (24) Stan, G.; Ciobanu, C. V.; Parthangal, P. M.; Cook, R. F. *Nano Lett.* **2007**, *7*, 3691.
- (25) Rabe, U.; Janser, K.; Arnold, W. *Rev. Sci. Instrum.* **1996**, *67*, 3281.
- (26) Yamanaka, K.; Nakano, S. *Jpn. J. Appl. Phys.* **1996**, *35*, 3787.
- (27) Stan, G.; King, S. W.; Cook, R. F. *J. Mater. Res.* **2009**, *24*, 2960.
- (28) Hurley, D. C.; Kopycinska-Müller, M.; Kos, A. B.; Geiss, R. H. *Meas. Sci. Technol.* **2005**, *16*, 2167.
- (29) Stan, G.; Cook, R. F. *Nanotechnology* **2008**, *19*, 235701.
- (30) Krylyuk, S.; Davydov, A. V.; Levin, I.; Motayed, A.; Vaudin, M. D. *Appl. Phys. Lett.* **2009**, *94*, No. 063113.
- (31) Any mention of commercial products in this article is for information only; it does not imply recommendation or endorsement by the NIST.
- (32) Johnson, K. L. *Contact Mechanics*, 6th ed.; Cambridge University Press: Cambridge, U.K., 1996; p 84.
- (33) Vlassak, J. J.; Nix, W. D. Indentation modulus of elastically anisotropic half-spaces. *Philos. Mag. A* **1993**, *67*, 1045.
- (34) Awaji, N.; Ohkubo, S.; Nakanishi, T.; Sugita, Y.; Takasaki, K.; Komiya, S. *Jpn. J. Appl. Phys.* **1996**, *35*, L67.
- (35) Kosowsky, S. D.; Pershan, P. S.; Krisch, K. S.; Bevk, J.; Green, M. L.; Brasen, D.; Feldman, L. C.; Roy, P. K. *Appl. Phys. Lett.* **1997**, *70*, 3119.
- (36) Cui, H.; Wang, C. X.; Yang, G. W. *Nano Lett.* **2008**, *8*, 2731.
- (37) EerNisse, E. P. *Appl. Phys. Lett.* **1977**, *30*, 290.
- (38) Kao, D. B.; McVittie, J. P.; Nix, W. D.; Saraswat, K. *IEEE Trans. Electron Devices* **1988**, ED-35-25.
- (39) Fukata, N.; Oshima, T.; Murakami, K.; Kizuka, T.; Tsurui, T.; Ito, S. *Appl. Phys. Lett.* **2005**, *86*, 213112.
- (40) Saada, A. S. *Elasticity theory and applications*, 2nd ed.; Krieger Pub. Co.: Malabar, FL, 1993; p 323.
- (41) Turley, J.; Sines, G. *J. Phys. D: Appl. Phys.* **1971**, *4*, 264.
- (42) Zhu, Y.; Xu, F.; Qin, Q.; Fung, W. Y.; Lu, W. *Nano Lett.* **2009**, *9*, 3934.
- (43) Ni, H.; Li, X.; Gao, H. *Appl. Phys. Lett.* **2006**, *88*, No. 043108.
- (44) Büttner, C. C.; Zacharias, M. *Appl. Phys. Lett.* **2006**, *89*, 263106.
- (45) Uematsu, M.; Kageshima, H.; Shiraishi, K.; Nagase, M.; Horiguchi, S.; Takahashi, Y. *Solid-State Electron.* **2004**, *48*, 1073.
- (46) Ohta, H.; Watanabe, T.; Ohdomari, I. *Jpn. J. Appl. Phys.* **2007**, *46*, 3277.
- (47) Dalla Torre, J.; Bocquet, J. L.; Limoge, Y.; Crocombette, J. P.; Adam, E.; Martin, G. *J. Appl. Phys.* **2002**, *92*, 1084.
- (48) Thurn, J.; Cook, R. F.; Kamarajugadda, M.; Bozeman, S. P.; Stearns, L. C. *J. Appl. Phys.* **2004**, *95*, 967.
- (49) Thurn, J.; Cook, R. F. *J. Mater. Sci.* **2004**, *39*, 4799.